Quantitative evaluation of attenuation contrast of X-ray computed tomography images using monochromatized beams

AKIRA TSUCHIYAMA,[1,*] KENTARO UESUGI,[2] TSUKASA NAKANO,[3] AND SUSUMU IKEDA[4]

[1]Department of Earth and Space Science, Osaka University, Toyonaka, 560-0043, Japan
[2]SPring-8/Japan Synchrotron Radiation Research Institute, Mikazuki, Hyogo Prefecture, 679-5198 Japan
[3]Geological Survey of Japan/National Institute of Advanced Industrial Science and Technology, Tsukuba, 305-8567 Japan
[4]Department of Complexity Science and Engineering, Graduate School of Frontier Sciences, The University of Tokyo, Kashiwanoha 5-1-5, Kashiwa, Chiba 277-8561, Japan

ABSTRACT

A quantitative relation between the linear attenuation coefficient (LAC) obtained by Synchrotron Radiation X-ray computed tomography (observed LAC) and the theoretically calculated LAC (theoretical LAC) of standard materials (minerals and metals) has been obtained for an X-ray microtomographic system at BL20B2 of SPring-8, Japan. This system, called SP-μCT, uses highly monochromatized and well-collimated X-ray beams produced by a synchrotron radiation source. Three-dimensional images were obtained for samples 0.4–4 mm in size at X-ray energies of 15–35 keV with a voxel size of $5.83 \times 5.83 \times 5.83\ \mu m^3$. A histogram of the observed LAC for each sample was well-fitted by a Gaussian curve except for heavy metals whose X-ray transmittance was insufficient. The contrast resolution of CT images is best (within 5% of the LAC value) at LACs of about 10–30 cm^{-1}. A garnet schist was imaged with SP-μCT to verify the observed–theoretical LAC relation for minerals contained in a rock sample. The result was consistent with the relation obtained for the standards. The CT and back-scattered electron images of the rock sample were compared. The present results put restrictions on discrimination of mineral phases and estimation of chemical compositions (e.g., Mg/Fe ratio) of certain minerals forming solid solutions based on CT values. The present quantitative relationship between observed and theoretical LACs enables us to obtain an absolute elemental concentration map by imaging just above and below the X-ray absorption edge energy of the element (subtraction method).

INTRODUCTION

X-ray computed tomography (CT) is a non-destructive method that provides cross-sectional images (CT images) of objects using X-ray attenuation. A CT image is expressed as a spatial distribution of so-called CT values, which correspond to the X-ray linear attenuation coefficient (LAC) of a material obtained by tomographic reconstruction. Three-dimensional (3-D) internal structures can be obtained by stacking successive CT images. The X-ray CT technique originally was developed for medical diagnosis (Hounsfield 1973; Ambrose et al. 1973). This technique has been applied to other fields including earth and planetary material science (e.g., Ketcham and Carlson 2001). Industrial and sometimes medical CT scanners have been used for earth and planetary materials: metamorphic rocks (e.g., Carlson and Denison 1992; Denison et al. 1997), sedimentary rocks (e.g., Wellington and Vineger 1987), igneous rocks (Philpotts et al. 1999; Ikeda et al. 2000), and meteorites (e.g., Arnold et al. 1993; Benedix et al. 2003). In recent years, high-resolution CT scanners with a spatial resolution greater than a few tens of micrometers have been used to analyze fine structures, such as fluid inclusions in minerals (Nakashima et al. 1997), sigmoidal garnets in a metamorphic rock (Ikeda et al. 2002), and microstructures of chondritic meteorites (Kondo et al. 1997).

A synchrotron radiation (SR) source provides tunable, monochromatized, and naturally collimated (parallel) X-ray beams that have many advantages for CT (Flannery et al. 1987; Bonse and Busch 1996). Monochromatized beams eliminate beam hardening, which causes CT image artifacts, and thus permit CT values to relate quantitatively to LACs. Furthermore, collimated beams readily yield 3-D images with high spatial resolution. Hirano et al. (1990) applied a SR microtomographic system at the Photon Factory in Japan to a meteorite sample, although they were unable to obtain 3-D images because they used a linear X-ray detector.

Uesugi et al. (1999, 2001) have developed an X-ray microtomographic system, named SP-μCT, using SR at SPring-8. The effective spatial resolutions of this system are about 13 μm at BL20B2 for samples smaller than 5 mm in diameter (Uesugi et al. 1999) and about 1.5 μm at BL47XU for samples smaller than 0.45 mm in diameter (Uesugi et al. 2001). SP-μCT has been applied to earth and planetary materials: chondrules and chondrites (Tsuchiyama et al. 2003a,b; Kusaka et al. 2001; Kitamura et al. 2003), micrometeorites (Tsuchiyama et al. 2001, 2003), symplectite in a peridotite (Morishita et al. 2003) and sands (Matsushima et al. 2004). 3-D element images were obtained by imaging objects just above and below the X-ray absorption edge energy of an element (the so-called "subtraction" method: e.g., Thompson et al. 1984) for Fe in a micrometeorite (Tsuchiyama et al. 2001) and Cs in a Cs-doped partially molten granite

---

132

(Ikeda et al. 2004). Other SR microtomographic systems have also been applied to Earth and planetary samples: e.g., by Rivers et al. (1999), Hertz et al. (2003), and Murray et al. (2003) at the Advanced Photon Source (APS) of Argonne National Laboratory, and by Lemelle et al. (2004) at the European Synchrotron Radiation Facility (ESRF).

The relationship between the CT value and LAC is not straightforward in almost all of the commercial X-ray CT scanners, where polychromatic X-ray beams are used. This is mainly due to the beam hardening effect, where the energy distribution spectra of the beams are modified through absorption as lower-energy X-rays are absorbed more strongly than higher-energy ones (Denison et al. 1997). Moreover, the term "CT value" has been used ambiguously in many cases. In particular, values that are modified by some correction in the reconstruction procedures are usually used as CT values (in addition, the correction method is usually not described). Such "ambiguous" CT values merely give relative values in an arbitrary unit.

Some quantitative relations between CT values and LAC were obtained under certain constraints to within a certain error margin using specific medical CT scanners for objects having LACs close to that of water (McCullough et al. 1974; McCullough 1975) and minerals (Tsuchiyama et al. 2000). Nakano et al. (1997) examined the relation between CT value and density using an industrial CT scanner with a high-energy X-ray source (3 MeV) for minerals and related materials. Tsuchiyama et al. (2002) quantified the relationship between CT value and LAC of minerals using an industrial high-resolution CT scanner for minerals with an accelerating voltage of 50–65 kV. They embedded samples within a silicon powder in a cylindrical container to reduce the beam hardening effect and calculated normalized CT values with an olivine standard of known chemical composition. However, the relation was scattered, especially for large LACs, mainly due to the inevitable beam hardening effect.

When monochromatic X-rays are used, beam hardening does not occur and, ideally, the CT value should be identical to LAC. However, they may not be exactly the same due to some non-ideality in an actual CT system. If we can quantify the relation between the two, we should be able to estimate materials, such as mineral species, from their CT values because LAC is a function of the chemical composition and the density of a material at a given X-ray energy. In addition, the concentration of an element can in some cases be obtained quantitatively by the subtraction method. Hirano et al. (1989, 1990) established the relation between CT value and LAC for certain standard materials at the Photon factory. However, their results only apply under a limited set of imaging conditions. Moreover, their CT values have an arbitrary unit. By contrast, the CT value provided by the tomographic reconstruction program used at SPring-8 directly estimates LAC. Thus, hereafter, the CT values in the present study, or LAC derived from tomographic reconstructions, will be called "observed LAC," whereas theoretically calculated LAC will be called "theoretical LAC."

In this study, the quantitative relation between observed and theoretical LACs has been obtained in a wide range of conditions by imaging standard materials of minerals and metals with SP-μCT at BL20B2 of SPring-8. A rock sample (garnet schist) was also imaged to verify the observed–theoretical LAC relation for minerals contained in a single sample. A back-scattered electron (BSE) image of a section of the rock was compared with the corresponding CT image. Although the observed–theoretical LAC relation obtained in this study is applicable only to SP-μCT at BL20B2, the present method for calibrating CT values or observed LAC is applicable to any X-ray CT system that utilizes monochromatic beams.

EXPERIMENTAL PROCEDURE

Standard samples and their imaging conditions are summarized in Table 1. The samples are single crystals of synthesized quartz, natural quartzite, high-purity amorphous silica, silica glass, and metal wires (Al, V, Ti, Fe and Ni). To evaluate an observed LAC, which is affected by the presence of the surrounding materials, some samples were embedded in Si or amorphous silica powder inside a cylindrical container of a plastic straw (about 4 mm in diameter).

Samples were imaged with SP-μCT at BL20B2 of SPring-8 (Uesugi et al. 1999). SP-μCT is composed of an X-ray source, a sample stage, and an X-ray beam monitor (Fig. 1). BL20B2 is a bending magnet beamline producing monochromatic X-rays with a flux density of $\sim 1 \times 10^9$ photons/s/mm²/100mA and narrow energy band pass ($\Delta E/E < 10^{-3}$, where E is the photon energy) by an Si (311) double-crystal monochromator (Goto et al. 2001). In some cases, the monochromator was detuned to reduce the effect of harmonics. In this study, however, the monochromator was not detuned because the harmonics detected in the absorption curves of a 3.5 μm thick Gd_2O_2S plate were small throughout a wide range of X-ray energies. Images of transmitted X-ray intensities through a sample were taken at X-ray energies of 15 to 35 keV by rotating the sample by 180 degrees with a rotational step angle of 1 to 0.125 degrees (180 to 1440 projections). Images of direct X-ray beams were measured with no sample for every ten transmitted images to correct for time decay of the X-ray intensity. Dark current of the detector system was measured before and after the CT measurement for correction of the images. All images were obtained by an X-ray detector, where the X-ray was transformed into visible light by a fluorescent screen (powder Gd_2O_2S:Tb, about 10 μm thick), expanded by a relay lens ($\times 2$) and subsequently detected by a cooled CCD camera (1000×1018 pixels; pixel size = 12 μm $\times$ 12 μm) with a dynamic range of 14 bits. The sample and fluorescent screen were positioned as close together as possible (5–6 mm) to avoid X-rays refracted by the sample. Imaging required 1 to 5 h depending on the X-ray energy and sample size. After the standard pre-processing of raw X-ray intensities and their logarithm conversions, CT images (1000×1000 pixels in full images) were reconstructed by a convolution back-projection algorithm (Nakano et al. 1997, 2000) with a Chesler's type convolution filter (Chesler and Riederer 1975). Nakano et al. (2000) carried out a systematic test for the computer program used in SP-μCT using simulated projection data, which were calculated from given LACs and sample shapes, and showed that the program can reconstruct the correct LACs except for a few pixel layers at the sample edges. 3-D structures were reconstructed by stacking 100–600 slice images. The size of each voxel (pixel in 3-D) in the 3-D images was 5.83 μm $\times$ 5.83 μm $\times$ 5.83 μm, and the effective spatial resolution was about 13 μm (Uesugi et al. 1999).

To verify the observed–theoretical LAC relation in a rock sample, a schist from Scotland containing sigmoidal garnet porphyroblasts (sample no. 80904 of Ikeda et al. 2002) was imaged using conditions similar to those employed for the standard samples. The sample was cut into a cylindrical shape (4.5 mm in diameter and 3.9 mm in height) to reduce CT image artifacts. The X-ray energy was 30 keV and the rotational step angle was 0.5 degrees (360 projections). The 3-D image was obtained from 700 slices. After imaging, the sample was cut, polished, and sectioned. The polished thin section was observed under a JEOL JSM-5510LV scanning electron microscope (SEM) at Osaka University.

Calculation of LAC

The theoretical linear attenuation coefficient (LAC), μ, of a sample was calculated using the following equation (e.g., McCullough 1975):

$$\mu = \rho \sum_i w_i \tau_i (E) \tag{1}$$

where ρ is the bulk density, w_i is the weight fraction of the i-th element, and τ_i is the mass attenuation coefficient (MAC) of the i-th element, which is a function of the photon energy, E. The values of ρ were adopted from references (see Table 1) except for the amorphous silica sphere and silica glass. These densities were measured by the buoyancy method with a balance (Sartorius MC1AC-MC). The procedure was the same as that followed by Tsuchiyama et al. (2000). MAC val-

TABLE 1. Imaging conditions and results for standard samples

Imaging no.	Energy keV	Expodure time s/projection	No. of projection	Sample	Shape	Size* mm	Peak position f_p, cm^{-1}	Characteristic width, Δf_p, cm^{-1}	Normalized residue, R	Theoretical LAC, μ, cm^{-1}	Density† ρ, g/cm³	γ‡	Δγ
001031a	20	8	360	aluminum	wire	5	8.240	0.8081	0.0493	9.287	2.698	0.8872	0.0870
001031b	20	8	360	aluminum	wire	2	8.354	0.3600	0.0071	9.287	2.698	0.8995	0.0388
001031c	20	8	360	aluminum	wire	1	8.370	0.3358	0.0095	9.287	2.698	0.9012	0.0362
001031d	20	4	360	aluminum	wire	0.5	8.305	0.4950	0.0160	9.287	2.698	0.8942	0.0533
010213b	20	5	720	aluminum	wire	2	8.234	0.3329	0.0048	9.287	2.698	0.8866	0.0358
010213c	25	8	1440	quartz‖	rod	4	3.209	0.2553	0.0025	3.663	2.648	0.8763	0.0697
010213c-1§	25	8	720	quartz‖	rod	4	3.208	0.2900	0.0029	3.663	2.648	0.8758	0.0792
010213c-2§	25	8	360	quartz‖	rod	4	3.207	0.3599	0.0051	3.663	2.648	0.8757	0.0983
010213c-3§	25	8	180	quartz‖	rod	4	3.191	0.4106	0.0138	3.663	2.648	0.8714	0.1121
010213d	25	8	720	quartz‖	piece	~3×2×1	3.051	0.3020	0.0040	3.663	2.648	0.8331	0.0825
010214c	25	7	720	quartz‖	piece**	~3×2×1	3.143	0.4426	0.0043	3.663	2.648	0.8582	0.1208
010214b	25	7	720	quartzite#	rod	4	3.290	0.3125	0.0051	3.663	2.648	0.8983	0.0853
010227f	25	10	450	quartzite#	rod	4	3.327	0.3556	0.0065	3.663	2.648	0.9083	0.0971
010214e	15	4	180	amorphous silica	sphere	2	11.103	0.6272	0.0208	12.742	2.199	0.8714	0.0492
010531e	25	10	360	silica glass	rod	4	2.778	0.2762	0.0070	3.046	2.201	0.9120	0.0907
010531f	25	10	360	silica glass	piece	~2×1×1	2.679	0.2855	0.0109	3.046	2.201	0.8794	0.0937
010531g	25	10	360	silica glass	piece**	~2×1×1	2.788	0.5254	0.0161	3.046	2.201	0.9151	0.1725
010531h	25	9	360	silica glass	piece††	~2×1×1	2.707	0.3365	0.0120	3.046	2.201	0.8887	0.1105
010227d	35	25	360	vanadium	wire	1	18.136	0.9489	0.0313	21.961	6.110	0.8258	0.0432
010227a	30	16	180	titan	wire	1	18.593	1.1526	0.0350	22.573	4.540	0.8237	0.0511
010214d	35	20	360	iron	wire	0.5	33.080	2.2535	0.0670	41.625	7.874	0.7947	0.0541
010227b	30	14	360	nickel	wire	0.4	61.095	13.0366	0.1665	92.047	8.910	0.6637	0.1416
010227c	35	25	360	nickel	wire	0.4	45.293	4.3429	0.0660	59.592	8.910	0.7600	0.0729

* Diameters of wire, rod, and shpere.
† Measured for amorphous silica and silica glass; Emsley (1991) for Al, V and Ti; Olhoeft and Johnson (1989) for quartz, Fe and Ni.
‡ CT value/LAC (f_p/μ).
§ CT images obtained for different numbers of projection from one imaging experiment with 1440 projections (010213c) by thinning out some projections.
‖ Synthesized by hydrothermal method.
From a Ryoke metamorphic zone (Sakuraiji, Nukata, Aichi Prefecture, Japan).
** Embedded in silicon powder.
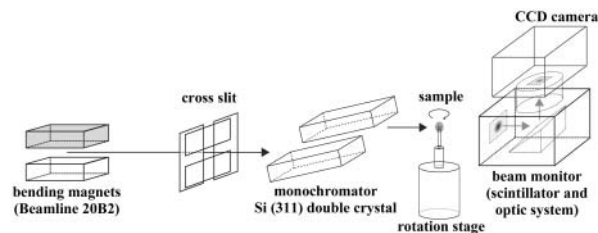†† Embedded in amorphous silica powder.

FIGURE 1. A schematic of the microtomographic system at BL20B2 of SPring-8 (SP-μCT) used in the present experiments.

ues for elements were used that include photoelectric absorption and elastic and Compton scatterings, as tabulated by Hubble and Seltzer (1996).

Image analysis procedure

Observed LACs in CT images were originally reconstructed as floating point numbers. They were converted to 8-bit values for image analysis in 3-D. In the CT images for the standards, the values of observed LAC corresponding to the theoretical LACs of air (0 cm^{-1}) and the sample were converted to values showing a brightness of 0 and 200 in the 8-bit image, respectively. Original software named SLICE was used for the image analysis. There are several commercial software packages for 3-D image analysis but their functions are insufficient for the specific purposes of the present study. SLICE is composed of a set of commands processing a 3-D image (successive TIFF files) under the UNIX operating system.

Sample regions of the standards were extracted by threshold and erosion operations. The median value of the theoretical LACs of air and the sample was adopted as the threshold. The extracted object was eroded by one voxel layer to eliminate blurring with the adjacent air. Minor changes in the values of the threshold and the number of eliminated voxel layers virtually did not affect the results of the image analysis on the observed LACs and further discussion. The sample region was manually selected when the samples were embedded in powders.

RESULTS

Standard materials

Figure 2 shows examples of CT images. No beam hardening artifacts were seen and the brightness was almost even for the homogeneous samples in most of the CT images (e.g., Fig. 2a). However, for some samples, where the X-ray beam was not transmitted sufficiently, the images were noisy and the sample edge was brighter than the interior (Fig. 2b). Faint rings, another type of CT image artifact, were observed (e.g., Figs. 2a, 2e, and 2f). When a single crystal was imaged, Bragg diffraction occurred over the whole sample at certain angles during sample rotation. This caused parallel sets of streaks in CT images (Fig. 2c). Grain boundaries were not observed in natural quartzite, where the grain size is on the order of a few hundred micrometers (Fig. 2d). This sample contains small inclusions of heavy minerals (white spots in Fig. 2d: probably opaque minerals like magnetite) and voids (black dots in Fig. 2d). A silica glass sample embedded in amorphous silica powder (Fig. 2e) is compared with one that has not been embedded (Fig. 2f).

To determine the characteristic value of observed LAC for each sample, a frequency distribution diagram, or histogram, of observed LAC for each set of 3-D images was constructed (Fig. 3). In this histogram, observed LACs at the peaks, f_p, ~0 cm^{-1} and >0 cm^{-1} correspond to air and the sample, respectively. The histogram of the extracted sample is well fitted by a Gaussian curve for most of the samples with sufficient X-ray transmittance (Figs. 3a and 3c–3f):
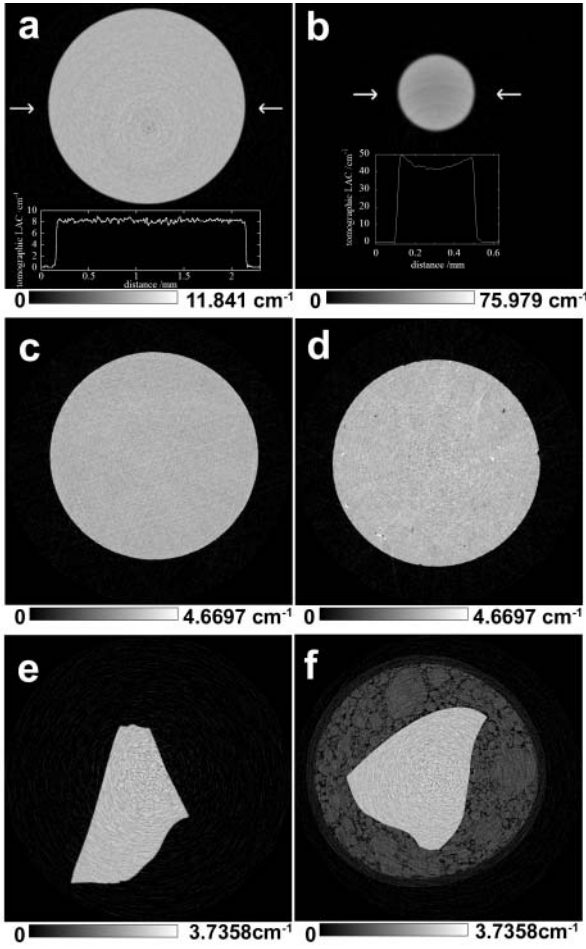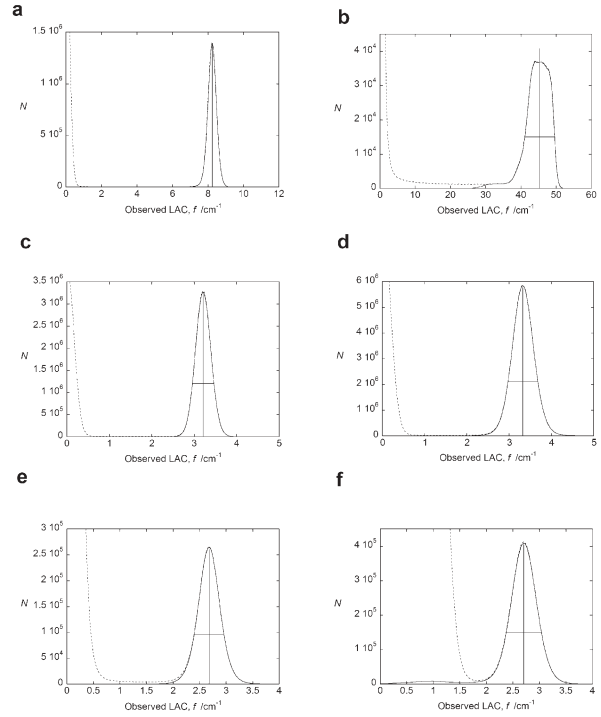
FIGURE 3. Histograms of observed LAC, f, for 3-D images of the standard materials. The samples are the same as in Figure 2. Dotted and solid curves correspond to histograms for the whole images and sample portions, respectively. The CT value of each sample peak position, f_p, with its peak height, N_p, (vertical line at the sample peak) and its characteristic width, $\pm \Delta f_p$ (horizontal line at the height of 1/e of the peak height), which are obtained by a Gaussian fit (Eq. 2), are shown for each sample.

FIGURE 2. CT images of standard materials. **(a)** Aluminum rod 2 mm in diameter (010213b, slice92: 20 keV). A line profile is superimposed between the arrows. **(b)** Nickel wire 0.4 mm in diameter (010227c, slice 149: 35 keV). A line profile is superimposed between the arrows. **(c)** Quartz rod 4mm in diameter (010213c, slice98: 25 keV). **(d)** Quartzite rod 4mm in diameter (010227f, slice254: 25 keV). The width of the image is 5.83 mm. **(e)** A piece of silica glass (010531f, slice189: 25 keV). **(f)** A piece of silica glass embedded into amorphous silica powder (010531h, slice127: 25 keV). Gray scales show the relation between observed LAC and shading intensity. The width of the images are **(a)** 2.92 mm, **(b)** 1.49 mm, **(c)** 5.83 mm, **(d)** 5.83 mm, **(e)** 4.08 mm and **(f)** 5.25 mm. Ring artifacts of varying severity are visible in some of the images.

$$N = N_p e^{-\left(\frac{f-f_p}{\Delta f_p}\right)^2} \qquad (2)$$

where N is the frequency, N_p is the frequency at the peak (peak height), f is the observed LAC, and Δf_p is the characteristic peak width that is equal to the half width of the peak at $N = N_p/e$, where e is the base of the natural logarithm. We used f_p as the characteristic value of the observed LAC for each sample. The results are summarized in Table 1. A parameter for the deviation from the Gaussian curve was defined as the normalized residue, R:

$$R = \sigma / N_p \qquad (3)$$

where σ is the square root of the mean squared difference between the histogram and the Gaussian curve. The peak shape deviates from a Gaussian curve for samples with insufficient X-ray transmittance (Fig. 3b). The tail of the sample peak at $f \sim 30$–35 cm^{-1} is due to improper selection of the sample region, which is caused by the bright sample edge (Fig. 2b) with the conventional threshold and the erosion number. The histograms of the sample peaks are almost identical for samples embedded and not embedded in powders (e.g., Figs. 2e and 2f). The large peak up to $f \sim$ 1.5 cm^{-1} for the whole sample histogram (dotted curve) in Figure 3f corresponds to the air and the surrounding amorphous silica powder. The small peak at $f \sim 1$ cm^{-1} is due to improper selection of the sample region, which was made manually. Different CT images were obtained for different numbers of projections from one imaging experiment with 1440 projections (010213c in Table 1) by thinning out some projections. As the number of projections decreases, Δf_p increases while f_p remains constant.

As already mentioned, observed and theoretical LAC values are ideally identical when monochromatic beams are used. However, the observed LAC, f_p, is slightly smaller than the theoretical LAC, μ, in the present experiments. The relation between f_p and μ is shown in Figure 4. If the non-linear response of the X-ray detector known as the gamma correction (Harrington 1987) is considered, f_p should be proportional to μ, as will be discussed in the next section. In fact, f_p is almost proportional to μ for small μ ($\mu < \sim 20$ cm^{-1}):
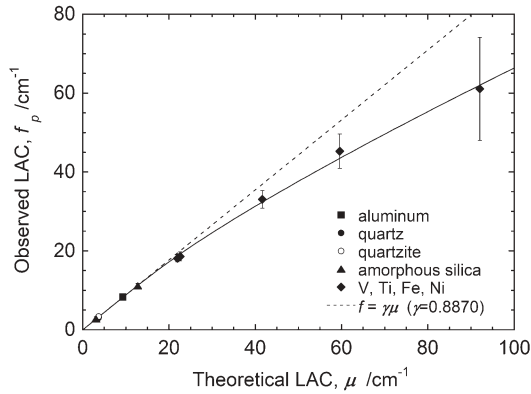
FIGURE 4. The characteristic values of observed LACs, f_p, of the samples plotted against their theoretical LACs, μ. The dotted line shows the linear f_p-μ relation with $\gamma = 0.8870$ in Equation 4. The values of f_p were obtained by Gaussian fitting of sample peaks in the observed LAC histograms. Error bars show the characteristic width of the sample peak, $\pm \Delta f_p$. The theoretical LACs were calculated from the chemical compositions, densities, and mass attenuation coefficients as a function of the photon energy using Equation 1.

$$f_p = \gamma \mu \qquad (4)$$

where the proportionality coefficient γ was determined by least-squares fitting ($\gamma = 0.8870 \pm 0.0039$). The linear relation does not hold for large μ ($\mu > \sim 20$ cm^{-1}), in which case f_p is almost proportional to a power of μ:

$$f_p = a\,\mu^b \qquad (5)$$

where coefficients of a and b were determined by least-squares fitting ($a = 1.505 \pm 0.243$ and $b = 0.8227 \pm 0.0385$). We can incorporate Equations 4 and 5 into the following empirical equation for the f_p-μ relation:

$$f_p = \left[\left(\gamma \mu \right)^m + \left(a \mu^b \right)^m \right]^{1/m} \qquad (6)$$

where the parameter m was determined by fitting ($m = -18.0$). The reverse equation is expressed as follows:

$$\mu = \left[\left(\delta f_p \right)^n + \left(c f_p^{\,d} \right)^n \right]^{1/n} \qquad (7)$$

where the parameters were determined by fitting as $\delta = 1.127 \pm 0.005$, $c = 0.5819 \pm 0.1414$, $d = 1.227 \pm 0.062$ and $n = 19.4$.

Contrast resolution of the CT images is represented by Δf_p. Figure 5 shows the $\Delta f_p/f_p$–f_p plot. $\Delta f_p/f_p$ attains its minimum value ($\sim 5\%$) at $f = 10$–30 cm^{-1} although the data are scattered for smaller f_p and the number of data points may not be sufficient for larger f_p. Observed LAC at the minimum might correspond to the optimal X-ray transmittance that minimizes the fluctuation in observed LAC or $\Delta f_p/f_p$.

Rock sample

Figure 6a shows a back-scattered electron (BSE) image of the garnet schist section. Despite our best efforts to make it so, the cutting plane did not turn out exactly parallel to the CT slices.
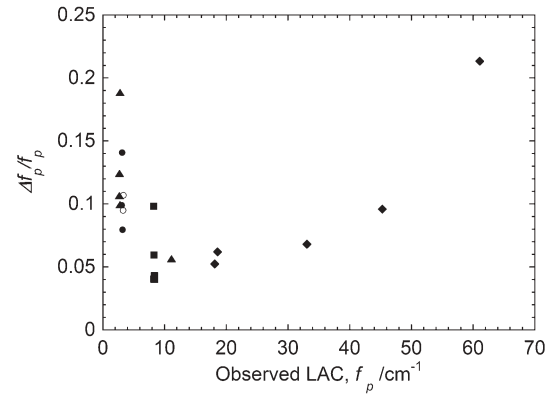

FIGURE 5. The degree of observed LAC fluctuation, $\Delta f_p/f_p$, plotted against the observed LAC, f_p. The legend is the same as that in Figure 4.
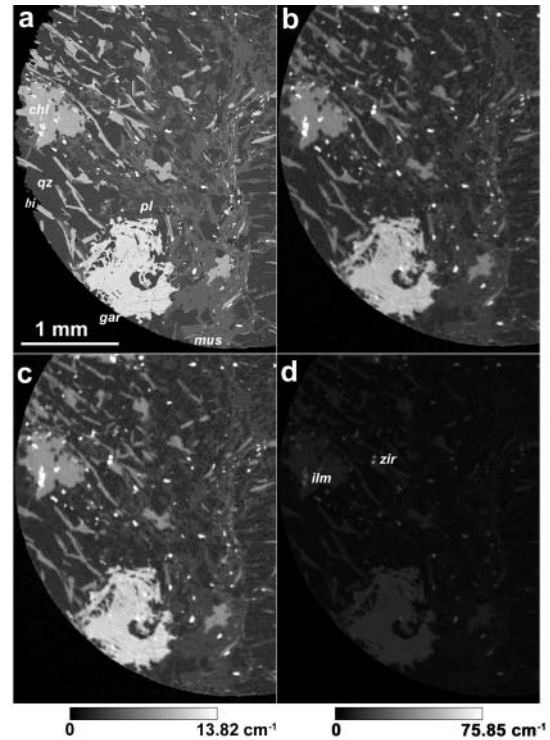

FIGURE 6. A cross-section of a garnet schist (sample no. 80904 of Ikeda et al. 2002). **(a)** A BSE image at minimum magnification. **(b)** The CT image corresponding to this BSE image. **(c)** A LAC image expressed in terms of μ converted from (b) using the observed–theoretical LAC relation of Equation 7. **(d)** The LAC image expressed in terms of μ under a different contrast. The gray scale on the left (0–13.82 cm^{-1}) is common to (b) for observed LAC and (c) for theoretical LAC. The gray scale on the right (0–75.85 cm^{-1}) corresponds to (d) for theoretical LAC. qz = quartz, pl = plagioclase, mus = muscovite, chl = chlorite, bi = biotite, gar = garnet, ilm = ilmenite, zir = zircon.

Therefore, a CT image as close as possible to the BSE image was obtained from the 3-D image by image processing with SLICE (Fig. 6b). Faint ring artifacts are seen in the CT image.

Quartz, plagioclase (An$_{15}$), muscovite, chlorite, biotite, garnet, ilmenite, and zircon are identifiable in the BSE image (Fig.

6a). In the CT image (Fig. 6b), however, plagioclase and chlorite cannot be distinguished from quartz and biotite, respectively. Figure 7a shows the observed LAC histogram for the 3-D image, where the peaks for quartz and plagioclase overlap, as do those for biotite and chlorite. In this histogram, the logarithm of the frequency, N, is plotted to show the major and minor minerals with different N values simultaneously. The characteristic values of observed LAC for quartz-plagioclase and garnet were identified from the peaks in the histogram whereas those for muscovite, chlorite-biotite, ilmenite, and zircon from the bumps (arrows in Fig. 7a). The theoretical LAC values of the minerals were calculated from their compositions (Table 1 of Ikeda et al. 2002). The observed-theoretical LAC plot (Fig. 7b) is consistent with the f_p-μ relation for the standards (Eqs. 6 or 7) within an error of 10%. This result shows that Equation 6 or 7 can be applied to the rock sample. The CT images in terms of f_p of the garnet schist were converted to LAC images expressed in terms of μ sing the present f_p-μ relation (Eq. 7). The images are shown in Figures 6c and 6d with different contrasts. The histogram of the 3-D LAC image is shown in Figure 7a.

DISCUSSION

Discrepancy between f_p and μ

As already mentioned, the reconstruction program is not the origin of the discrepancy between f_p and μ. Moreover, systematic measurements of the projection data (its definition is given below in Eq. 9) of high-purity metal wires with circular cross sections show that a similar discrepancy exists between the measured and theoretical projection data. Thus, the $f_p - \mu$ discrepancy stems from factors before the image reconstruction, such as: (1) the non-linear response of the X-ray detector, (2) scattering of X-ray beams, and/or (3) harmonic wave beams generated by the monochromator.

If we assume that:

$$J \propto I^\gamma \qquad (8)$$

where J is the intensity of a visible light detected at the CCD camera (Fig. 1), I is the net X-ray intensity, and γ is a constant, the linear $f_p - \mu$ relation (Eq. 4) can be explained (see Appendix). This relation is widely used as the gamma correction for the brightness of a computer display (Harrington 1987). Recently, the observed–theoretical LAC relation at BL47XU of SPring-8 was also determined for small samples (<0.45 mm) with higher spatial resolution (~1.5 μm) (Nakamura et al. 2003). The relation is almost linear as expressed by Equation 4 as long as f_p <400 cm⁻¹ ($\gamma = 0.892 \pm 0.004$). This γ value is same as that for f_p <20 cm⁻¹ in the present study within the error.

A change in f_p is expected for large μ (Eq. 5) if we consider that the scattering X-ray beam cannot be ignored for samples with insufficient X-ray transmittance. The X-ray transmittance is represented by projection, p:

$$p = \ln\left(\frac{I_0}{I}\right) = \int \mu ds = \mu S \qquad (9)$$

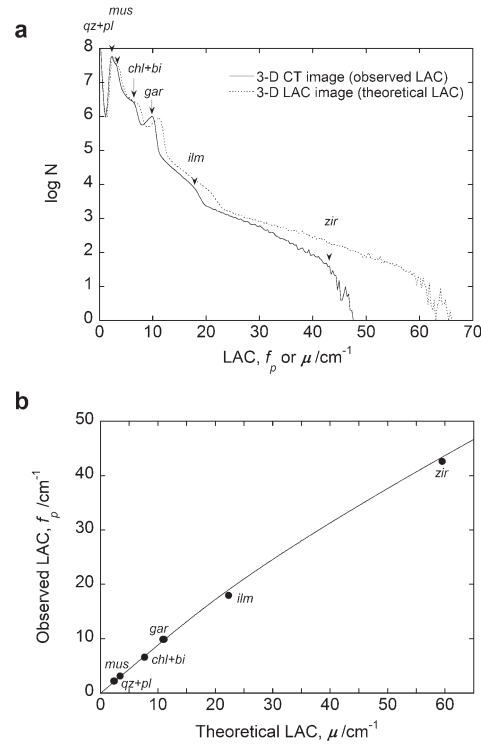where I_0 and I are the intensities of the incident and transmit-

FIGURE 7. (a) Histograms for 3-D CT and LAC images of a garnet schist (sample no. 80904 of Ikeda et al. 2002). The logarithm of the frequency is plotted to show the major (qz = quartz, pl = plagioclase, mus = muscovite, chl = chlorite, bi = biotite, gar = garnet) and minor minerals (ilm = ilmenite, zir = zircon) simultaneously. **(b)** Characteristic values of observed LAC for the minerals vs. their theoretical LAC values. The f_p-μ relation for the standard materials (Eqs. 6 or 7) is shown as a solid line.

ted X-ray beams, respectively, s is the coordinate in the sample along the X-ray beam paths, and S is the sample thickness (a homogeneous sample is assumed). If the scattered X-ray beam intensity, I_s, is assumed to be superimposed on I homogeneously, the f_p/μ ratio becomes (see Appendix):

$$\frac{f_p}{\mu} = -\frac{\gamma}{p}\ln\left(e^{-p} + \frac{I_s}{I_0}\right) \qquad (10)$$

If I_s is negligibly small compared with I_0 ($I_s/I_0 \ll 1$), Equation 10 reduces to Equation 4. If I_s is not negligibly small, f_p/μ decreases with increasing p for large p [$p \gg -\ln(1 - I_s/I_0)$]. This may explain Equation 5 qualitatively. However, the f_p/μ-p plot (Fig. 8) shows that f_p/μ does not decrease simply with increasing p (f_p/μ ~0.9 at large p for some samples: Al wire 5 mm in diameter at 20 keV and amorphous silica sphere at 15 keV). In this plot, the values of p were calculated from the maximum widths of the samples (e.g., the diameter of a rod was adopted as S in Eq. 9). At present, we do not know exactly why f_p/μ decreases with increasing μ but not p. Heterogeneous distribution of I_s (e.g., I_s near the edge of a sample might be larger than the interior on a projection image) may be responsible for the f_p-μ-p relation. Alternatively, beam hardening by X-ray beams with higher monochromator harmonics may affect f_p. Indeed, the bright contrast near the sample edge in CT images of samples with insufficient X-ray
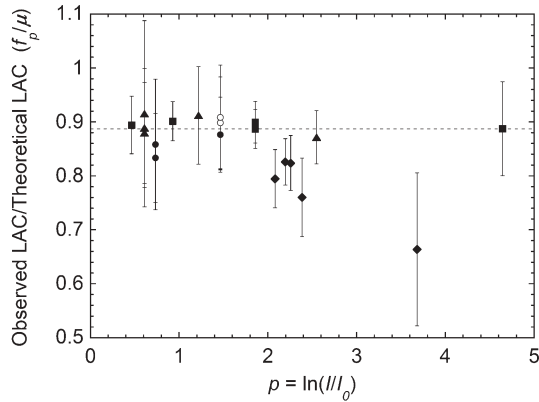
FIGURE 8. The ratio between the characteristic observed LAC and theoretical LAC (f_p/μ) plotted against the projection, p (Eq. 9). The legend is the same as that in Figure 4.

FIGURE 9. A histogram of CT, LAC, and BSE images of a cross section of Figure 6. The arbitrary scale for the BSE brightness was set so that the peak positions for quartz-plagioclase and garnet coincided with those of the CT image. The frequencies were normalized by the peak height for quartz-plagioclase.

transmittance (Fig. 2b) may be due to a kind of beam hardening induced by harmonics. The physical meaning of the f_p-μ relation (Eqs. 6 or 7) is not entirely clear at present.

Comparison of CT and BSE images of the rock sample

Rock textures are commonly examined by BSE images under an SEM. The brightness of a BSE image is related to the mean atomic number of a material whereas that of a CT image is related to the X-ray attenuation. As the two types of images are similar in many cases, they were compared in this study.

Figure 9 shows the histogram of observed LAC in the CT image of the garnet schist section of Figure 6b together with that of the brightness of the BSE image (8-bit gray scale) of Figure 6a. As brightness has an arbitrary scale and unit, the brightness scale was set so that the peak positions for quartz-plagioclase and garnet of the BSE image coincided with those of the CT image. The frequencies were also normalized by the peak height for quartz-plagioclase. The muscovite peak was distinct from the quartz-plagioclase peak in the BSE image. The peak width for each mineral of the CT image is larger than that of the BSE image. This shows that the CT image has poorer contrast resolution than the BSE image. The two images differ with respect to their spatial resolution as well. The CT image quality is also affected by ring artifacts.

Strictly speaking, the brightness of BSE images is given by the backscatter coefficient of the material, η, which can be expressed as $\eta = \Sigma w_i\eta_i$ where η_i is the backscatter coefficient of the i-th element (Hall and Lloyd 1981; Dilks and Graham 1985):

$$\eta_i = -0.0256 + 0.016Z_i - 1.86 \times 10^{-4}Z_i^2 + 8.3 \times 10^{-7}Z_i^3 \quad (11)$$

where Z_i is the atomic number of the i-th element. The η values for the minerals in the garnet schist were calculated from their compositions. A plot of the BSE brightness and η for the minerals (Fig. 10a) shows that the relation is almost linear, at least for the BSE imaging system of the SEM used in the present experiment. A plot of the BSE brightness and observed LAC shows that the relation can be represented by a convex curve (Fig. 10b). The contrast resolution of the BSE image is better than those of CT
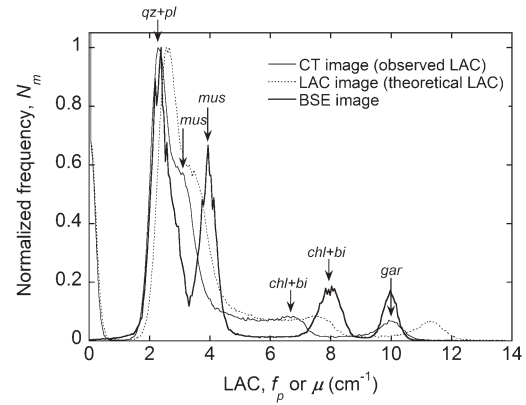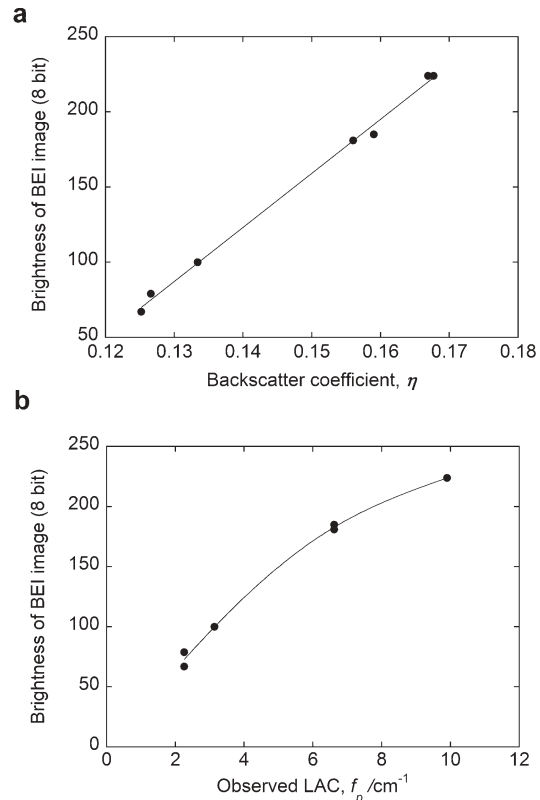

FIGURE 10. (a) A plot of the brightness of the BSE image of Figure 6a (8-bit gray scale) vs. backscatter coefficient, η, for quartz, plagioclase, muscovite, chlorite, biotite, and garnet (core and rim). **(b)** A plot of the BSE brightness vs. the characteristic values of observed LAC, f_p, for the minerals in Figure 7.

images as already mentioned, and the convex curve shows that the difference is greater for lighter minerals (quartz, plagioclase, and muscovite) than for heavier ones (biotite or chlorite and garnet). However, CT imaging has its advantage too: it allows 3-D structures of samples to be obtained non-destructively.

Estimation and discrimination of minerals by CT value

Based on the present f_p-μ relation, we can impose certain constraints on the identification of materials, such as mineral species, in CT images obtained using SP-μCT at BL20B2. Using Equation 6, the theoretical LACs of important minerals in terrestrial rocks and meteorites were calculated and converted to observed LACs, f, for SP-μCT at BL20B2. These values at 30 keV were plotted against the backscatter coefficient, η, calculated using Equation 11 (Fig. 11a). We adopted 30 keV for the observed LACs as the typical photon energy for imaging at BL20B2. It should be noted that the relative values of LAC among minerals are almost independent of photon energy as long as no absorption edge energies are crossed. As seen in Figure 11a, the η-f relation is roughly represented by a convex curve as in Figure 10b, once again demonstrating that the contrast resolution advantage of BSE images is more pronounced for lighter minerals. The η-f relation is redrawn for minerals related to granitic, metamorphic, and sedimentary rocks (Fig. 11b), mafic to ultramafic rocks (Fig. 11c), and chondritic meteorites (Fig. 11d). Figure 11b shows that we cannot distinguish albite from quartz and anorthite from orthoclase in CT images as $\Delta f_p/f_p$ is

>10% at $f_p\sim$2–3 cm^{-1} (Fig. 5). Though enstatite and quartz have similar observed LAC, they are easily distinguished if the Fs component is included in orthopyroxene. The situation is similar for the Ca-free Mg-amphibole (anthophylite) and Mg, Al-garnet (pyrope). The Ca-Mg end-members of pyroxene (diopside) and amphibole (tremolite), can be distinguished from their Ca-free counterparts (enstatite and anthophyllite).

If olivine and pyroxenes have similar Mg numbers (~0.9), olivine and orthopyroxene cannot be distinguished from each other but they can be distinguished from clinopyroxene (Fig. 11c). Olivine and orthopyroxene may be distinguished if they are Fe-rich. Magnetite and chromite should be distinguishable as $\Delta f_p/f_p\sim$5% at $f_p\sim$20 cm^{-1}.

The CT values of minerals found in CAIs (Ca- and Al-rich inclusions) of chondrites (forsterite, spinel, hibonite, anorthite, diopside, and melilite), are roughly in the 2.5–5 cm^{-1} range (Fig. 11d). As these values overlap with those of Mg-rich mafic minerals (Fo$_{70-100}$, En$_{10-60}$, and Di$_{80-100}$) and plagioclase, it is difficult to distinguish CAIs from the bulk of chondrules without any textural information. Figure 11a shows that Fe-Ni metal is easily distinguished from Fe sulfides or magnetite. Discrimination
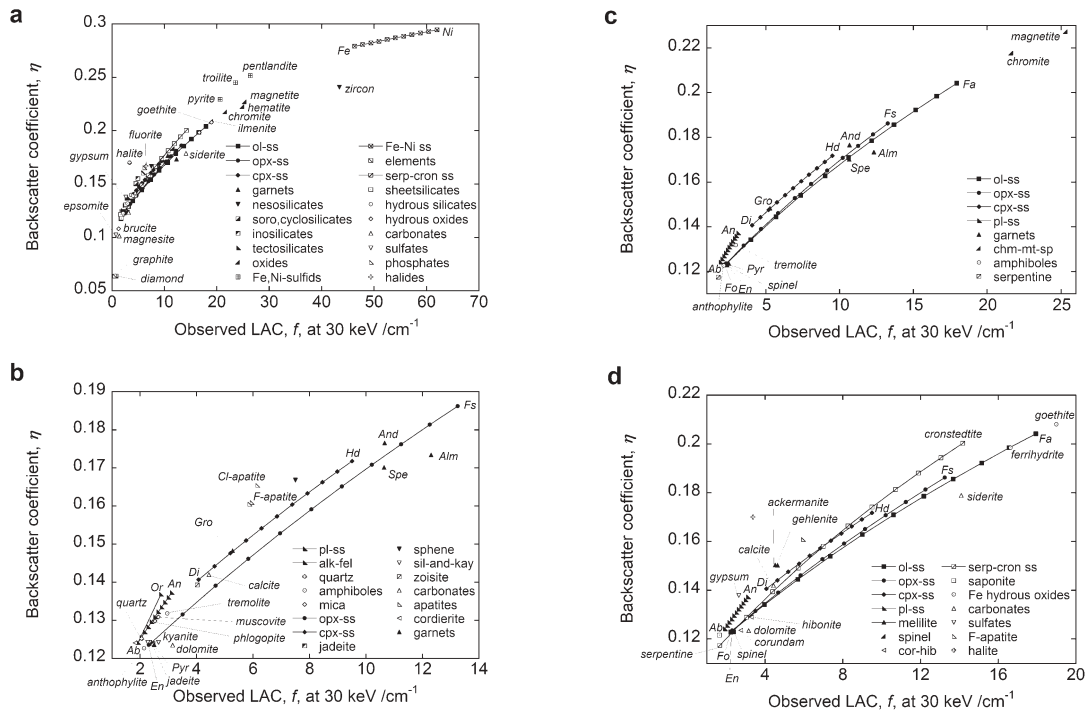

FIGURE 11. A plot of backscatter coefficient, η, vs. observed LAC, f, at 30 keV for minerals of interest. **(a)** A general trend. Minerals with solid solutions (olivine, orthopyroxene, clinopyroxene, and Fe-Ni metal) are shown at 20 mol% increments (e.g., at a Fo content of 100, 80, 60, 40, 20, and 0). Fe-bearing serpentine is also shown by assuming a solid solution of Mg-serpentine and cronstedtite. Garnets: pyrope (Pyr), almandine (Alm), spessartine (Spe), grossular (Gro), and andradite (And). Nesosilicates: β-Mg$_2$SiO$_4$, γ-Mg$_2$SiO$_4$, andalusite, sillimanite, kyanite, sphene, and zircon. Soro- and cyclosilicates: akermanite, gehlenite, and cordierite. Inosilicates: MgSiO$_3$-perovskite, jadeite, and wollastonite. Tectosilicates: anorthite, albite, orthoclase, and quartz. Oxides: chromite, magnetite, spinel, corundum, hematite, ilmenite, rutile, and hibonite. Fe-Ni sulfides: pyrite, troilite, and pentlandite. Elements: diamond and graphite. Sheet silicates: talc, phlogopite, muscovite, kaolinite, and saponite. Hydrous silicates: prehnite, zoisite, anthophyllite, and tremolite. Hydrous oxides: brucite, goethite, and ferrihydrite. Carbonates: calcite, dolomite, gypsum and siderite. Sulfates: gypsum, and epsomite. Phosphates: fluorapatite, chrolapatite, and hydroxyapatite. Halides: fluorite and halite. **(b)** Minerals found in granitic, metamorphic, and sedimentary rocks. Plagioclase solid solution is shown at 20 mol% increments. **(c)** Minerals found in mafic and ultramafic rocks. **(d)** Minerals found in chondritic meteorites.

between troilite and magnetite is difficult whereas that between troilite and pentlandite may be possible.

As shown in Figure 11, f and η are largely dependent on the concentrations of heavy elements, such as Fe. If the mineral species are known in advance, we can estimate their compositions (e.g., the Mg/Fe ratios) from the qualitative observed LACs. It should be noted that the Fe/Ni ratios estimated from the observed LAC values have large errors due to the large $\Delta f_p/f_p$ value at large observed LACs. Substitutions involving heavy elements, such as U, Th, and REEs, may affect mineral identification or compositional estimation for major-element solid solutions using observed LACs. For example, a heavily metamict zircon from Sri Lanka contains 1.14, 0.174, 0.373, and 0.084 wt% Hf_2O, Dy_2O_3 + $Er_2O_3+Yb_2O_3$, U_2O, and Th_2O, respectively, and 253 ppm Pb (Geisler et al. 2002). Comparison of theoretical LACs between zircon with and without these heavy elements shows that the relative difference of the LACs is only 0.8–1.5% at X-ray energies of 20–50 keV, the range of energies typically used at BL20B2 of SPring-8. Apatite is another example of a phase containing such heavy elements. At X-ray energies of 20–50 keV, the relative difference between the LACs of apatite with and without heavy elements is 0.9–1.0% for 50, 100, and 50 ppm U, Th, and Pb, respectively, and 0.1 wt% REE_2O_3 (Dy was used as REE in the calculation), and 6.4–7.1% for the same concentrations of U, Th, and Pb and 1 wt% REE_2O_3. As these relative differences are smaller than or similar to the contrast resolution ($\Delta f_p/f_p$) of the present experiments (Fig. 5), such substitutions virtually do not affect the observed LACs as long as the heavy element concentrations are low. Pores and/or inclusions in minerals smaller than the spatial resolution of CT images may also affect the observed LACs. The contrast resolution (Fig. 5) shows that a porosity of less than 5% does not affect the observed LACs by SP-μCT at BL20B2.

Estimation of mineral phases and solid-solution compositions as discussed above is potentially useful for precious samples that cannot be cut, such as cultural assets and fragile or porous samples that are easily damaged. This technique is also useful for curation of extraterrestrial materials, such as precious meteorites and samples returned by planetary missions [e.g., Hayabusa mission to S-type asteroid Itokawa by JAXA (Kawaguchi et al. 2003)].

Element image by subtraction method

The distribution of an element can be obtained by imaging immediately above and below the X-ray absorption-edge energies of the element and taking the difference between the two images (e.g., Thompson et al. 1984). In the subtraction method, the weight fraction of element i, w_i, can be obtained from the following equation:

$$w_i = \frac{\Delta\mu}{\rho\Delta\tau_i} \tag{12}$$

where $\Delta\mu$ is the difference of LACs between the two energies, ρ is the bulk density, and $\Delta\tau_i$ is the difference of MACs (mass attenuation coefficients) of the element i between the two energies. However, as $\Delta\mu$ is generally different from the observed LAC difference, the concentrations cannot be obtained directly by subtraction between the two sets of CT images. If the CT images at the two energies can be converted into images expressed in terms of theoretical LACs using the f_p-μ relation, we can obtain images expressed in terms of $\Delta\mu$ ($\Delta\mu$ images). Ikeda et al. (2004) obtained a 3-D Cs image of a partially molten Cs-doped granite sample with SP-μCT at BL20B2 of SPring-8 using the present f_p-μ relation (Eq. 7). They obtained $\Delta\mu$ images from the two sets of CT images and, based on the $\Delta\mu$ image, the element image [$w(Cs)$ image] by measuring $\Delta\tau(Cs)$ and assuming a certain value for ρ. They further cut the sample and obtained a Cs map of the section with an electron microprobe analyzer. The Cs concentration distribution in the $w(Cs)$-image was almost identical to that in the Cs map. This result strongly suggests that the empirical f_p-μ relation is generally useful to CT images taken with SP-μCT at BL20B2.

SUMMARY

A quantification of linear attenuation coefficients (LACs) obtained by X-ray computed tomography (observed LAC) is now possible for SP-μCT at BL20B2 of SPring-8 using the observed LAC (f_p) – theoretical LAC (μ) relation obtained in the present study. Although the present results can only be used for a specific CT system (SP-μCT at BL20B2), similar f_p-μ relations could be obtained for other CT systems using monochromatic beams. Additional studies are necessary to elucidate the physical meaning of the observed–theoretical LAC relation and to confirm that the relation applies to a wide rage of imaging conditions. Recently, the observed–theoretical LAC relation at BL47XU of SPring-8 was also determined for small samples (<0.45 mm) with higher spatial resolution (~1.5 μm) (Nakamura et al. 2003). This could yield the Fe concentrations in the 3-D Fe image of an Antarctic micrometeorite (Tsuchiyama et al. 2001). Estimation of densities of samples that are so small that their masses cannot be measured even by an ultra-microbalance may be feasible, as well as discrimination of minerals and estimation of solid-solution compositions. The present study brings a new perspective to quantification of the attenuation contrast of CT images obtained by the X-ray CT technique using monochromatized beams.

REFERENCES CITED

Ambrose, J. (1973) Computerized transverse axial scanners (tomography), 2. clinical application. British Journal of Radiology, 46, 1023–1047.
Arnold, J.R., Resta, J.P. Jr., Friedman, P.J., and Kambic, G.X. (1982) Computed tomographic analysis of meteorite inclusions. Science, 219, 383–384.
Benedix, G.K., Ketcham, R.A., McCoy, T.J., and Wilson, L. (2003) Vesiculation in ordinary chondrites due to impact melting: the "PAT" 91501 answers. Lunar Planet. Sci., XXXIV, Abstract no. 1947, Lunar and Planetary Institute, Houston (CD-ROM).
Bonse, U. and Busch, F. (1996) X-ray computed microtomography (μCT) using synchrotron radiation (SR). Progress in Biophysics and Molecular Biology, 65, 133–169.
Carlson, W.D. and Denison, C. (1992) Mechanisms of porphyroblast crystallization: Results from high-resolution computed tomography. Science, 257, 1236–1239.

Chesler, D.A. and Riederer, S.J. (1975) Ripple suppression during reconstruction in transverse tomography. Physics and Medical Biology, 20, 632–636.

Denison, C., Carlson, W.D., and Ketcham, A. (1997) Three-dimensional quantitative textural analysis of metamorphic rocks using high-resolution computed X-ray tomography: Part I. Methods and techniques. Journal of Metamorphic Geology, 15, 29–44.

Dilks, A. and Graham, S.C. (1985) Quantitative mineralogical characterization by back-scattered electron image analysis. Journal of Sedimentary Petrology, 55, 347–355.

Emsley, J. (1991) "The elements" 2nd edition,.251 p. Clarendon Press, Oxford.

Geisler, T, Pidgeon, R.T., van Bronswijk, W., and Kurtz, R. (2002) Transport of uranium, thorium, and lead in metamict zircon under low-temperature hydro-thermal conditions. Chemical Geology, 191, 141–154.

Flannery, B.P., Deckman, H.W., Roberge, W.G., and D'Amico, K.L. (1987) Three-dimensional X-ray microtomography. Science, 237, 1439–1444.

Goto, S., Takeshita, K., Suzuki, Y., Ohashi, H., Asano, Y., Kimura, H., Matsushita, T., Yagi, N., Isshiki, M., Yamazaki, H., Yoneda, Y., Umetani, K., and Ishikawa, T. (2001) Construction and commissioning of a 215-m-long beamline at SPring-8. Nuclear Instruments and Methods in Physics Research A, 467, 682–685.

Hall, M.G. and Lloyd, G.E. (1981) The SEM examination of geological samples with a semi-conductor backscattered electron detector. American Mineralogist, 66, 362–368.

Harrington, S. (1987) Computer graphics: a programming approach, 2nd. ed., 466 p. McGraw-Hill, New York.

Hertz, J., Ebel, D.S., and Weisberg, M.K. (2003) Tomographic study of shapes and metal abundances of Renazzo chondrules. Lunar and Planet. Science Conference, XXXIV, Abstract no. 1959, Lunar and Planetary Institute, Houston (CD-ROM).

Hirano, T., Eguchi, S., and Usami, K. (1989) Study of quantitative elemental analysis of monochromatic X-ray CT using synchrotron radiation. Japanese Journal of Applied Physics, 28, 135–139.

Hirano, T., Funaki, M., Nagata, T., Taguchi, I., Hamada, H., Usami, K., and Hayakawa, K. (1990) Observation of Allende and Antarctic meteorites by monochromatic X-ray CT based on synchrotron radiation. Proceedings of NIPR Symposium on Antarctic Meteorites, 3, 270–281.

Hounsfield, G.N. (1973) Computerized transverse axial scanning (Tomography), Part 1. description of system. British Journal of Radiology, 46, 1016–1022.

Hubbell, J.H. and Seltzer, S.M. (1996) Tables of X-Ray Mass Attenuation Coefficients and Mass Energy-Absorption Coefficients from 1 keV to 20 MeV for Elements $Z = 1$ to 92 and 48 Additional Substances of Dosimetric Interest. (NIST, Physical Laboratory, Physical Reference Data. http://physics.nist.gov/PhysRefData/XrayMassCoef/cover.html)

Ikeda, S., Nakano, T. and Nakashima, Y. (2000) Three-dimensional study on the interconnection and shape of crystals in a graphic granite by X-ray CT and image analysis. Mineralogical Magazine, 64, 945–959.

Ikeda, T., Shimobayashi, N., Wallis, S.R., and Tsuchiyama, A. (2002) Crystal-lographic orientation, chemical composition and three-dimensional geometry of sigmoidal garnet: evidence for rotation. Journal of Structural Geology, 24, 1633–1646.

Ikeda, S., Nakano, T., Tsuchiyama, A., Uesugi, K., Suzuki, Y., Nakamura, K., Nakashima, Y., and Yoshida, H. (2004) Nondestructive three-dimensional element-concentration mapping of a Cs-doped partially molten granite by X-ray computed tomography using synchrotron radiation. American Mineralogist, 89, 1304–1312.

Kawaguchi, J., Uesugi, K., and Fujiwara, A. (2003) The MUSES-C mission for the sample and return-its technology development status and readiness. Acta Astronautica, 52, 117–123.

Ketcham, A. and Carlson, W.D. (2001) Acquisition, optimization and interpretation of X-ray computed tomographic imagery: application to the geosciences. Computational Geosciences, 27, 381–400.

Kitamura, M., Tsuchiyama, A., Nakano, T., and Uesugi, K. (2003) Three-dimensional structures of metal-sulfide grains in CO chondrites: formation of metal-sulfide chondrules (abstract). Meteoritics and Planetary Science, 38, Supplement, A52.

Kondo, M., Tsuchiyama, A., Hirai, H., and Koishikawa, A. (1997) High resolution X-ray computed tomographic (CT) images of chondrites and a chondrule. Antarctic Meteorite Research, 10, 437–447.

Kusaka, H., Tsuchiyama, A., Noguchi, T., Uesugi, K., and Nakano, T. (2001) Three-dimensional structure of a radial pyroxene chondrule using X-ray microtomography (abstract), Antarctic Meteorites, XXVI, 66–68.

Lemelle, L., Simionovici, A., Truche, R., Rau, C., Chukalina, M., and Gillet, P. (2004) A new nondestructive X-ray method for the determination of the 3D mineralogy at the micrometer scale. American Mineralogist, 89, 547–553.

Matsushima, T., Saomoto, H., Uesugi, K., Tsuchiyama, A., and Nakano, T. (2004) Detection of 3-D irregular grain shape of Toyoura sand at SPring-8, X-ray

CT for Geomaterials. In Ohtani and Obara, Eds., Proceeding of International workshop on X-ray CT for geomaterials, Balkem, p. 121–126.

McCullough, E.C. (1975) Photon attenuation in computed tomography. Medical Physics, 2, 307–320.

McCullough, E.C., Baker H.L., Houser O.W., and Resse, D.F. (1974) An evaluation of the quantitative and radiation features of a scanning X-ray traverse axial tomography: The EMI scanner. Radiography, 111, 709–715.

Morishita, T., Tsuchiyama, A., Nakano, T., and Uesugi, K. (2003) Observation of three-dimensional microstructures of symplectite minerals in the Horoman Peridotite Complex using a high-resolution X-ray CT system at SPring-8.Chishitugaku Zasshi, 109, III–IV.

Murray, J., Beesenburg, J.S., and Ebel, D.S. (2003) Unambiguous voids in Allende chondrules and refractory inclusions. Lunar and Planetary Science Conference, XXXIV, Abstract no. 1999, Lunar and Planetary Institute, Houston (CD-ROM).

Nakano, T., Nakamura, K., Someya, T. and Ohtsuka, H. (1997) Observation of 3-dimensional internal structures of rock using X-ray CT: (1) density calibration of CT value (in Japanese with English abstract). Geoinformatics, 8, 239–255.

Nakano, T., Nakashima Y., Nakamura, A., and Ikeda, S. (2000) Observation and analysis of internal structure of rock using X-ray CT (in Japanese with English abstract). Journal of Geolical Society of Japan, 106, 363–378.

Nakamura, K., Tsuchiyama, A., Nakano, T., and Uesugi, K. (2003) Quantitative evaluation of the relation between X-ray linear attenuation coefficient and CT value, and its application to 3-D element distribution of micrometeorites. Abstract of the International Symposium on Evolution of Solar System Materials: A New Perspective from Antarctic Meteorites, 97–98.

Nakashima, Y., Hirai, H., Koishikawa, A., and Ohtani, T. (1997) Three-dimensional imaging of arrays of fluid inclusions in fluorite by high-resolution X-ray CT. Neues Jarbuch fur Mineralogie Monatshefte, 559–568.

Olhoeft, G.R. and Johnson, G.R. (1989) Densities of rocks and minerals, in R.S. Carmichael, Ed., Practical Handbook of Physical Properties of Rocks and Minerals, p. 141–176. CRC press, Inc., Boca Raton.

Philpotts, A.R., Brustman, C.M., Shi, J., Carlson, W.D., and Denison, C. (1999) Plagioclase-chain networks in slowly cooled basaltic magma. American Mineralogist, 84, 1819–1829.

Rivers, M.L., Sutton, S., and Eng, P. (1999) Geoscience application of x-ray computed microtomography. Proceedings of SPIE, Developments in X-Ray Tomography II, 3772, 78–86.

Thompson, A.C., Llacer, J., Campbell Finman, L., Hughes, E.B., Otis, J.N., Wilson, S., and Zeman, H.D. (1984) Computed tomography using synchrotron radiation. Nuclear Instruments and Methods in Physics Research, 222, 319–323.

Tsuchiyama, A., Hanamoto, T., Nakashima, Y., and Nakano, T. (2000) Quantitative evaluation of attenuation contrast of minerals by using a medical X-ray CT scanner. Journal of Mineralogical and Petrological Sciences, 95, 125–137.

Tsuchiyama, A., Uesugi, K., Noguchi, T., Yano, H., Nakano, T., and Suzuki, Y. (2001) Three-dimensional microstructures of Antarctic micrometeorites by X-ray computed tomography using synchrotron radiation at SPring-8. Meteoritics and Planetary Science, 36, Suppl. A210.

Tsuchiyama, A., Nakamura, T., Nakano, T., and Nakamura, N. (2002) Three-dimensional description of the Kobe meteorite by micro X-ray CT method: possibility of three-dimensional curation of meteorite samples. Geochemical Journal, 36, 369–390.

Tsuchiyama, A., Shigeyoshi, R., Kawabata, T., Nakano, T., Uesugi, K., and Shirono, S. (2003a) Three-dimensional structures of chondrules and their high-speed rotation. Lunar and Planetary Science Conference, XXXIV, Abstract no. 1271, Lunar and Planetary Institute, Houston (CD-ROM).

Tsuchiyama, A., Osada, Y., Nakano, T., and Uesugi, K. (2003b) Experimental reproduction of classic barred olivine chondrules: open system behavior and thermal history of chondrule formation. Geochimica et Cosmochimica Acta., in press.

Uesugi, K., Tsuchiyama, A., Nakano, T., Suzuki, Y., Yagi, N., Umetani, K., and Kohmura, Y. (1999) Development of micro-tomography imaging system for rock and mineral samples (presented at the SPIE Conference on Developments in X-Ray Tomography II, Denver, Colorado, July, 1999). Proceedings of Society of Photo-Optical Instrumentation Engineers, 3772, 214–221.

Uesugi, K., Suzuki, Y., Yagi, N., Tsuchiyama, A., and Nakano, T. (2001) Development of high spatial resolution X-ray CT system at BL47XU in SPring-8. Nuclear Instruments and Methods in Physics Research A, 467–468, 853–856.

Wellington, S.L. and Vineger, H.J. (1987) X-ray computerized tomography. Journal of Petroleum Technology, 39, 885–898.

See Appendix next page

APPENDIX: DERIVATION OF EQUATIONS 4 AND 10

The actual projection detected by the CCD camera in the beam monitor, P_j, can be expressed as:

$$P_j = \ln\left(\frac{J_0}{J}\right) = f_P S, \tag{A1}$$

where J_0 is the incident intensity. A homogeneous sample is assumed. When we use Equations 8 and 9, then:

$$P_j = \ln\left(\frac{I_0}{I}\right)^{\gamma} = \gamma \mu S. \tag{A2}$$

Equation 4 is derived by comparing Equations A1 and A2.

When the scattered X-ray beam is superimposed homogeneously on the transmitted X-ray beam, P_j becomes:

$$P_j = \ln\left(\frac{I_0}{I + I_S}\right)^{\gamma}. \tag{A2'}$$

On the other hand, combining Equations A1 and 9 yields

$$P_j = \frac{p f_p}{\mu}. \tag{A3}$$

Equation 10 is derived by comparing Equations A2', A3, and 9:

$$\frac{f_p}{\mu} = \frac{\gamma}{p}\ln\left(\frac{I_0}{I + I_S}\right) = -\frac{\gamma}{p}\ln\left(e^{-p} + \frac{I_S}{I_0}\right). \tag{10}$$

This equation is valid when the incident beam intensity is greater than the apparent transmitted beam ($I_0 \gg I + I_S$). This condition is equivalent with $e^{-p} + I_S/I_0 \ll 1$, or $p \gg -\ln(1 - I_S/I_0)$.